A DIELECTRIC-BASED, GeV/m CROSSED-LASER-BEAM ELECTRON LINEAR ACCELERATOR*

Yenchieh Huang and Robert L. Byer
Edward L. Ginzton Laboratory, Stanford University
Stanford, California 94305-4085

ABSTRACT

The acceleration gradient of a conventional RF accelerator is limited to about 50 MeV/m. To generate TeV electrons for next generation high energy physics, an RF accelerator would require a distance exceeding 20 km. In this paper, we propose a dielectric-based, multistaged, laser-driven electron linear accelerator operating in a vacuum that is capable of providing 1 TeV electrons in 1 km. Our study shows that GeV/m gradient and luminosity of $\sim 10^{33}\ \mathrm{cm}^{-2}\cdot\mathrm{sec}^{-1}$ are achievable using two focused crossed-laser beams, repeated every 330 μm, operated at a peak laser power of 0.2 GW per accelerator stage, a repetition rate of ~ 30 kHz, and an energy density of less than $2\ J/\mathrm{cm}^2$ on optical components for 100 fsec laser pulses. Cylindrical focusing shows a higher acceleration gradient than spherical focusing under the same laser damage threshold on optical components. Our three-dimensional computer simulations indicate superior electron beam characteristics from the proposed accelerator structure. The accelerator structure can be fabricated on silicon substrates by using modern lithographic technology.

*This manuscript represents the second of two lectures on "Laser Technology and Astrophysics" given by R. L. Byer at the 1994 Summer School.

©R. Byer 1994

TABLE OF CONTENTS

1. Introduction

2. Theoretical Background

3. Crossed-Laser-Beam Acceleration

    3.1 Single-Stage Accelerator Structure

    3.2 Acceleration Fields and Phases

    3.3 Energy Gain and Acceleration Gradient

    3.4 Multistage Accelerator Structure

4. Computer Simulations

    4.1 Energy Gain and Energy Spread

    4.2 Emittance and Multistage Trajectory Stability

    4.3 Phase Cancellation and Group Velocity Control

5. Laser Requirements and Luminosity

6. One-Dimensional Laser Focusing

    6.1 Acceleration Fields and Phases

    6.2 Average Acceleration Gradient

    6.3 Fabrication Techniques

7. Summary

1. Introduction

The maximum acceleration gradient of an RF accelerator is primarily limited by the structure breakdown under intense RF fields. In a conventional S-band RF accelerator, field emission on the copper wall occurs when the peak acceleration gradient reaches ~100 MeV/m (Ref. 1). The average acceleration gradient of an RF accelerator is thus limited to about 50 MeV/m. To reach the TeV energy region desired for the next linear collider using presently existing RF schemes requires tens of kilometers of accelerator structure.

The evolution of the RF driven linear accelerator over the past 50 years has been remarkable. The first accelerator constructed by Hansen at Stanford in 1949, which was only of 1 m length, led in successive stages to SLAC and energy levels in excess of 30 GeV. However, as noted by Livingston[2] in the early 1960s, the end of one technology for generating higher energies is often succeeded by a new technology for acceleration to greater energy levels. We believe that the laser source, coupled to a dielectric-based accelerator lattice operating in a vacuum, is now ready to lead the way to TeV energies in kilometer-length structures.

Thirty years after its invention, the laser has recently seen unprecedented advances in efficiency, peak power, average power, and stability. It now appears that solid state lasers driven by 40% efficient laser diode arrays will meet the peak and average power levels required for laser acceleration. These levels, as shown in this paper, are peak powers of 0.2 GW at 100 fsec pulses at ~ 30 Hz repetition rate for each of ~ 10^6 successive focal zones.

With the rapid advance of laser technology, one can obtain terawatt-class, pulsed solid-state lasers at the required efficiency and average power. Diode-pumped solid state lasers bring additional advantages of solid state reliability and a high electrical efficiency of 10%, with the potential of approaching 20% (Ref. 3). The laser accelerator gradient, like the RF accelerator gradient, is limited by damage. Figure 1(a) shows the damage fluence in J/cm^2 of dielectric[4] and copper[5] surfaces vs. laser pulse length, τ_p. The threshold damage fluence for dielectric is about an order of magnitude higher than that for copper.

Given the surface damage fluence and pulse lengths shown in Fig. 1(a), Fig. 1(b) shows the breakdown electric field on the material surface given by

$$E_s = \sqrt{\frac{2\eta \mathrm{J}}{\tau_p}},$$

where J is the surface damage fluence, and $\eta = 377\ \Omega$ is the wave impedance in vacuum. The surface field strength in Fig. 1(b) is the maximum acceleration gradient for a laser-driven linear accelerator set by the damage limit.

With the evidence in Fig. 1(b), laser acceleration using dielectric boundaries is the most probable scheme for achieving GeV/m gradients and for building future TeV electron accelerators at existing laboratory sites. Laser sources that may meet the peak and average power requirements at the 100 fsec10--psec pulse width are indicated on the same plot. From a laser engineer's point of view, a Ti:Sapphire laser is ideal for generating femtosecond pulses but may not be as efficient as other solid-state lasers for generating peak and average power in the picosecond regime. The acceleration gradient scaling vs. pulse length is discussed in Sec. 5.

In addition to building TeV-class accelerators within a manageable distance, laser acceleration has several desirable features:

1. High repetition rate: terawatt-class, mode-locked lasers can operate at a few tens of kilohertz. A high repetition rate means high average beam brightness and high luminosity for experiments. A high repetition rate also allows active feedback for the control of the accelerator structure alignment.
2. Short electron bunch: an ultrashort electron pulse on the order of one femtosecond is formed in each optical cycle. In synchrotron radiation or undulator radiation, the radiation power is linearly proportional to the electron current if the electron bunch length is longer than the radiation wavelength, whereas it is proportional to the square of the number of electrons when the bunch length is comparable or shorter than the radiation wavelength. Ultrashort electron bunch generated coherent radiation also allows researchers to explore ultrafast phenomena in various disciplines of science.
3. Simplicity and compactness: a laser accelerator uses off-the-shelf, bench-top laser sources and does not require bulky and costly high-voltage modulators and pulse-forming networks. Its high acceleration gradient opens the possibility of building

micro free-electron lasers or miniature MeV accelerators for hospital and industrial applications.

In this paper, we present the theoretical background for laser acceleration. We then analyze the proposed crossed-laser-beam accelerator structure and evaluate its feasibility with current laser technology. In obtaining the GeV/m gradient, we take into account several practical considerations such as laser damage, the drift space occupied by optical components, fabrication tolerance, and radiation loss. We also present three-dimensional particle simulation studies which demonstrate the ensemble behavior of electrons in a laser-driven linear accelerator.

2. Theoretical Background

One laser-acceleration approach is to duplicate the guided wave RF accelerator but on the scale of an optical wavelength. Zheng and Byer[6] have evaluated a guided wave laser accelerator approach based on a rectilinear dielectric waveguide driven by 100 fsec laser pulses. They have shown this approach satisfies the requirements for energy and momentum conservation. However, it requires submicron feature sizes and submicron electron beam sizes, and may be susceptible to electron damage and/or laser beam damage. In their evaluation of the dielectric guided wave structure, Zheng and Byer noted the limitation that damage places on the acceleration gradient and recognized the advantages of a dielectric-based structure.

In this paper, we extend the idea of a dielectric-based accelerator structure to a "semi-open" dielectric accelerator structure. We were led to this idea by noting that historically, the accelerator structures mimic the structure of the oscillators that produce the radiation. The semi-open dielectric structure resembles the laser resonator structure which is many wavelengths in length. The structure consists of a series of symmetrically focused laser beams at an angle to the electron beam in a geometry similar to that proposed by Haaland.[7] The evolution is significant in that it provides for higher gradient, symmetrically accelerated electron bunches, and the potential for using modern lithography as the tool of choice to fabricate the structure at a precision and cost that are acceptable.

Although nonlinear acceleration techniques such as inverse FEL, stimulated Compton scattering, or vacuum beat wave[8] allow electron acceleration in vacuum, the

electron's transverse motion causes severe radiation loss when the electron energy approaches GeV energy levels. It is now recognized that accelerators based on linear interaction with an electric field are the only approach for accelerating electrons to the TeV energy level.

Linear-acceleration schemes include the two-beam accelerator,[9,10] the plasma beat wave accelerator,[11] the inverse Cherenkov accelerator,[12] and the inverse Smith-Purcell accelerator.[13] The two-beam accelerator, which uses RF power generated from a low-energy beam, has reached an ~ 80 MeV/m gradient with a good efficiency. The plasma beat-wave accelerator, which uses two laser beams with a difference frequency close to the plasma frequency, produced a peak acceleration gradient of several GeV/m in a micro interaction zone. However, the complexity of generating the beat waves, and confining and multistaging the plasma imposes difficulties for achieving a GeV/m average gradient over a long distance. The proposed inverse Cherenkov and Smith-Purcell accelerators are not suitable for highly relativistic electrons because the phase matching requires that the ratio of the longitudinal electrical field (in the direction of electron acceleration) to the transverse field be proportional to $1/\gamma$, where γ is the electron energy normalized to its rest energy.

Free-space acceleration using laser beams is an appealing scheme, although it has been a subject of controversy in the literature. The main point of controversy relates to the Lawson-Woodward (LW) theorem[14,15] which rules out the possibility of a net energy gain for a relativistic electron interacting linearly with electromagnetic waves in an unbounded vacuum. Edighoffer and Pantell[16] pointed out that a plane-wave synthesized Gaussian beam, which is commonly used for describing optical beams, obeys the LW theorem, and that to achieve net acceleration, the laser beam must be terminated. Although Hauser *et al.*[17] and Haaland[7] calculated a significant energy gain for an electron traversing a laser focal zone over an indefinite distance, their analysis was incomplete in that they did not take into account the electrical field component in the propagation direction of the laser beam. Sprangle *et al.*[8] later corrected the mistake in Refs. (7) and (17) and proved that a crossed-laser-beam accelerator obeys the LW theorem. In other words, an electron may acquire a net energy from an electromagnetic wave via a linear process if the interaction length is finite.

Another area of controversy is the legitimacy of using the Gaussian beam formulas,[18] which do not satisfy Maxwell's equations exactly, for analyzing laser acceleration.[16] Sprangle *et al.* justified the use of the Gaussian beam formulas under the paraxial approximation. We adopted Sprangle's methodology for our analysis in this paper.

To our knowledge, very few people have proposed accelerator structures suitable for laser acceleration. Scully[19] proposed a simple laser LINAC structure using the longitudinal field of a high order Gaussian mode or a transversely shifted fundamental Gaussian mode. However, further analysis is needed on the effects of the laser damage and the transverse field components, and on the failure of the paraxial approximation when the laser spot size is comparable to the wavelength.

The phase velocity of an electromagnetic (EM) wave in vacuum is always larger than the electron velocity. Therefore, termination of the electromagnetic fields is necessary before the phase of the electromagnetic wave slips ahead of the electron by π for net acceleration to occur. Pantell and Piestrup[20] pointed out that energy exchange can occur within the π phase slip constraint. Steinhauser and Kimura later applied this argument to their axicon accelerator.[21] One example of energy transfer that is not phase matched is the microwave electron gun[22] in which electrons starting from thermal velocities slip in phase by $\sim \pi$ in the first gun cell and move into the second cell to catch another acceleration phase. In the following analysis for the crossed-laser-beam electron linear accelerator (LINAC), we terminate the laser fields after a finite interaction length which avoids the restriction of the LW theorem.

A laser beam can be focused in one or two transverse dimensions. For two-dimensional focusing, we present an acceleration analysis for on-axis electrons in Sec. 3, computer simulation in Sec. 4, and the corresponding laser requirements in Sec. 5. We then delineate the advantages of one-dimensional focusing in Sec. 6.

3. Crossed-Laser-Beam Electron LINAC

Propagating an electron through a laser focal zone at an offset angle to achieve electron acceleration by the tilted laser polarization was proposed in Refs. (17) and (20). Haaland[7] and Sprangle[8] further discussed the crossed-laser-beam configuration that symmetrically

cancels the two transverse laser fields while adding the two longitudinal fields along the electron axis.

In this section, we present the basic theory, propose an optical configuration for the crossed-laser-beam accelerator, and calculate its energy gain and average acceleration gradient within the limit set by laser damage.

3.1 Single-Stage Accelerator Structure

Figure 2(a) shows the proposed crossed-laser-beam accelerator geometry, wherein an electron traverses the focal zone at an angle θ with respect to the two laser beams. The insert in Fig. 2(a) defines the coordinates used in this paper. The unprimed coordinate system is the laboratory frame which includes the electron velocity axis, z. The primes indicate the rotated coordinates of the laser beams. The two laser beams are derived from a single laser source. They carry equal power and are phased such that on the z axis, the transverse fields (in x and y) cancel and the longitudinal fields (in z) add. A crossed-laser-beam accelerator employs the fundamental Gaussian mode and does not have the complexity of generating or transporting high order modes as does an axicon accelerator.[21] The accelerator uses repetitive dielectric boundaries over a distance no greater than a π phase slip between the laser field and the electron in a vacuum. Figure 2(b) shows the proposed accelerator optical configuration for a single-stage accelerator. Two laser beams are back-coupled from the $\pm x$ directions into the *microstage* using two prisms.

In general, the fabrication of a high reflection (HR) coating is more complex than making antireflection (AR) coating. The total internal reflection (TIR) inside the prisms permits the use of AR coating for beam coupling. For a prism made of fused silica or silicon nitride, the incident angle at the TIR face is approximately 45° for a small θ. Two high-reflectivity coated flat mirrors provide a secondary deflection and direct the two laser beams into the center of the microstage. The double-deflection, back-coupled scheme allows the coupling points [labeled A and A′ in Fig. 2(b)] on the prisms to be away from the z axis so that the laser beam clipping at the prism edges can be alleviated. This scheme allows a small crossing angle θ at a maximum optical fluence on the HR flat mirror. Beam clipping at the prism sets the geometrical beam coupling condition:

$$3\, l \times \theta > w, \tag{1}$$

where l is half of the interaction length measured from the focal point, and w is the Gaussian beam electric field beam radius at A and A′. Equation (1), to be discussed below, gives an allowed operational geometry for a specified acceleration gradient. Using TIR prisms permits the removal of the dielectric material between the prism and the flat mirror, which reduces the Cherenkov radiation loss. The structure is constant in y and thus allows cylindrical focusing if necessary. The electron beam aperture must be small compared to the laser beam size. For a small angle θ, a minimum prism width (in z) of 2 w is required for coupling ~ 90% of the laser power into the structure. Thus, the minimum drift space per microstage, where no laser fields exist, is approximately 2 w.

3.2 Acceleration Fields and Phases

For a linearly polarized fundamental Gaussian beam with a vector potential in x' focused in the x' and y', the field components in phasor notation can be cast as[23]

$$E_{x'} = \sqrt{\frac{2}{\pi}} \frac{\sqrt{2\eta P}}{w(z')} \exp[-jkz' + j\Phi(z') - jk\frac{x'^2 + y'^2}{2R(z')}] \times \exp[-\frac{x'^2 + y'^2}{w^2(z')}], \tag{2a}$$

$$E_{y'} = \left(\frac{-4x'y'/w_0^2}{k^2 w_0^2} \times \frac{z'^2/z_r^2 - 1 - 2j\,z'/z_r}{(z'^2/z_r^2 + 1)^2} \right) \times E_{x'}, \tag{2b}$$

$$E_{z'} = \frac{-2\,x'/w_0}{kw_0} \frac{z'/z_r - j}{(1 + z'^2/z_r^2)} E_{x'}, \tag{2c}$$

$$B_{y'} = \frac{1}{c} E_{x'}, \tag{2d}$$

$$B_{z'} = \frac{-2\,y'/w_0}{ckw_0} \frac{z'/z_r - j}{(1 + z'^2/z_r^2)} E_{x'}, \tag{2e}$$

where c is the free-space velocity of light, k is the free-space wave number, w_0 is the laser waist size, $z_r = \frac{\pi w_0^2}{\lambda}$ is the optical Rayleigh length, $w(z') = w_0\sqrt{1 + z'^2/z_r^2}$ is the $1/e$ laser field radius at z', $R(z') = z' + \frac{z_r^2}{z'}$ is the radius of curvature of the wavefront at z', and $\Phi(z') = \tan^{-1}(\frac{z'}{z_r})$ is the Guoy phase shift due to diffraction. The Guoy phase, in

addition to the usual plane wave phase, gives a π phase shift from $z' = -\infty$ to $z' = \infty$ for a focused laser beam.[24] For a tightly focused laser beam, the Guoy phase varies quickly about $z' = 0$ and can cause phase mismatch between the electron and the laser fields in a distance shorter than a Rayleigh length, as will be shown below.

The field components given above are derived under the paraxial approximation, $1/kw_0 << 1$. When x' and y' are normalized to w_0 and z' is normalized to the optical Rayleigh length, $E_{x'}$ and $B_{y'}$ are the zero-order expansion terms in $1/kw_0$, $E_{z'}$ and $B_{z'}$ are the first-order expansion terms, and $E_{y'}$ is the second-order expansion term. Since $E_{y'}$ is the second-order expansion term, the field variation in y' (or equivalently y) is nearly independent of the focusing, giving the opportunity of accelerating more electrons in the y dimension by using cylindrical focusing as will be discussed below.

With the appropriate coordinate transformation,

$$x' = x\cos\theta - z\sin\theta, \tag{3a}$$

$$y' = x\sin\theta + z\cos\theta, \tag{3b}$$

the resulting on-axis electrical field, summed from $E_{x'}$ and $E_{z'}$ of the two crossed laser beams, is

$$E_z = -4\sqrt{\frac{\eta P}{\pi}}\frac{\sin\theta}{w_0(1+\xi^2\cos^2\theta)}\exp\left[-\frac{(\xi\sin\theta/\theta_d)^2}{1+\xi^2\cos^2\theta}\right]\times\cos(\phi_p+\phi_g+\phi_r), \tag{4a}$$

where $\theta_d = w_0/z_r$ is the far-field diffraction angle, $\xi = z/z_r$ is the z coordinate normalized to the Rayleigh length, and ϕ_p, ϕ_g, ϕ_r are the plane wave phase, Guoy phase, and radial phase, respectively. For a relativistic electron with an energy γ and a small crossing angle $\theta << 1$, the three phase terms are

$$\phi_p = \omega t - kz\cos\theta \approx \frac{kz}{2}(\theta^2 - \frac{1}{\gamma^2}), \tag{4b}$$

$$\phi_g = 2\times\tan^{-1}\xi, \tag{4c}$$

$$\phi_r = -\frac{\xi(\theta/\theta_d)^2}{1+\xi^2}. \tag{4d}$$

The small angle assumption, carried out through this paper, is necessary for achieving phase coherence over a distance much longer than an optical wavelength. It is worth noting that an additional Guoy phase shift, contributed from summing $E_{x'}$ and $E_{z'}$, imposes the need of laser field truncation in the near field region.

Figure 3(a) shows the three phase terms (assuming $\theta/\theta_d = 1$ and $1/\gamma^2 << \theta^2$). The sum of the plane wave phase and radial phase terms is $\phi_p + \phi_r = \frac{\xi(\theta/\theta_d)^2}{1+\xi^2}$, which has the same sign as the Guoy phase term. Since the Guoy phase term, $2\times\tan^{-1}\xi$, produces a π phase shift from $-z_r$ to $+z_r$, net acceleration is possible only if the laser field is terminated for $z < |z_r|$. Figure 3(b) shows the normalized axial field seen by a relativistic electron for the same crossing angle as in Fig. 3(a). It is seen that an electron remains in phase and gains energy over approximately one Rayleigh length.

3.3 Energy Gain and Acceleration Gradient

Based upon the Gaussian field expressions in Eqs. (2a)--(2e), the energy gain over a distance from $-l$ to $+l$ for an on-axis, highly relativistic electron traversing through the two crossed Gaussian laser beams is given by[8]

$$\Delta W(\text{MeV}) = 87.6\sqrt{P(\text{TW})}\,\frac{1}{\xi\theta}\exp\left[-\frac{(\xi\theta)^2}{1+\xi^2}\right]\times\sin\left[\frac{\xi\theta^2}{1+\xi^2}\right], \qquad (5)$$

where P is laser power in terawatts, and $\xi = \frac{l}{z_r}$ is the interaction length normalized to the optical Rayleigh length. To derive Eq. (5), Eq. (4b) was approximated by $\phi_p \approx \frac{kz}{2}\theta^2$ under the assumption $1/\gamma^2 << \theta^2$. Thus for Eq. (5) to be valid, the injection electron energy must exceed a minimum energy $W_{\min}$ given by (in units of the electron rest mass)

$$W_{\min} = \frac{1}{\theta}. \qquad (6)$$

Electrons with an injection energy lower than $W_{\min}$ quickly fall out of phase due to the velocity slip.

For an unbounded interaction length from $-\infty$ to $+\infty$, the energy gain calculated from Eq. (5) reduces to zero, as the LW theorem predicts. We show by careful evaluation of Eq. (5) that the maximum energy gain for a microstage is

$$\Delta W_{\max}(\mathrm{MeV}) = 30\sqrt{P(\mathrm{TW})}, \tag{7}$$

when P is the peak laser power in terawatts, and $\theta = 1.37$ and $\beta = 0.46$ correspond to a π phase shift between the laser fields and the electron. At this time, 0.1 TW pulsed solid-state lasers are commercially available at modest cost. The maximum energy gain using this type of laser is about 10 MeV per acceleration stage.

In addition to the geometrical constraint in Eq. (1), laser damage on mirrors also sets a limitation on the acceleration gradient. As seen in Fig. 1(b), the gradient depends on the laser pulse length. A short laser pulse is desirable to obtain a high acceleration gradient. For example, with a 100 fsec pulse length, the damage threshold intensity is about $I_{\max} = 20\mathrm{TW}/\mathrm{cm}^2$, at a damage threshold fluence of ~ $2J/\mathrm{cm}^2$ (Ref. 4). The maximum laser power $P_{\max}$ at the damage threshold intensity $I_{\max}$ is given by

$$P_{\max} = I_{\max}\frac{w^2\pi}{2}, \tag{8}$$

where $\frac{w^2\pi}{2}$ is the area of the Gaussian laser beam on the HR mirror. For example, taking the laser spot size to be $50\,\mu\mathrm{m}$, one can drive the accelerator with $P_{\max}$ = 1.6 GW of laser peak power using 100 fsec pulses.

In practice, the critical parameter is not the maximum energy gain per microstage but the average acceleration gradient. We define the average acceleration gradient as the energy gain per stage, ΔW, divided by the length of an accelerator stage, $L_\mu = 2l + 2w$. Substituting (8) into (5) and dividing (5) by the accelerator microstage repeat distance L_μ, one obtains the average acceleration gradient under the laser damage constraint:

$$G = \left.\frac{\Delta W}{L_\mu}\right|_{P = I_{\max} w^2\pi/2}. \tag{9}$$

In Eq. (9), the variables are the interaction length $2l$, the laser waist radius w_0, the crossing angle θ, and the optical wavelength λ. Since solid state lasers at $\lambda \approx 1$ μm such

as Nd:YAG, Yb:YAG, Nd:YLF, and Nd:Glass give good stability, high efficiency, high peak power, and short optical pulses, we assume $\lambda = 1$ μm for the rest of our calculations.

Figure 4 shows the average acceleration gradient vs. the interaction length per stage $2l$, for $w_0 = 20$ μm and $\theta = 100$ mrad, 70 mrad, and 40 mrad. When the interaction length equals zero, the average gradient is reduced to zero instead of converging to the electric field strength at the focal point, because a finite drift distance of $2w$ per stage is taken into account in Eq. (9). For $\theta = 100$ mrad and 70 mrad, average gradients of more than 1 GeV/m are predicted for an interaction length in the range of 25 to 150 μm per microstage. In the same plot, a smaller angle, $\theta = 40$ mrad, gives a maximum average gradient of ~ 0.7 GeV/m. Note that for $\theta = 40$ mrad, the acceleration gradient is relatively insensitive to the interaction length, which can be as long as ~ 300 μm. The insensitivity to the interaction length at a certain laser beam crossing angle may be an advantage in accelerator design. For example, a larger structure size eases the manufacture process, reduces the radiation loss, allows a larger electron channel, and opens the fabrication tolerance. For these reasons, in the following we analyze a structure that provides $G \approx 0.7$ GeV/m.

For an accelerator fabricated to meet a certain acceleration gradient, θ and w_0 are the two variables that can be adjusted. Figure 5 shows the intersection of the geometric constraint given by Eq. (1) and the accelerator average gradient given by Eq. (9). As seen in Fig. 5, for the assumed 0.7 GeV/m average gradient, the contour circles shrink as the interaction length $2l$ increases, because (1) a longer $2l$ requires a smaller θ to maintain phase coherence, and (2) a small w_0 introduces too much Guoy phase shift while a large w_0 (and thus a large w) reduces the acceleration gradient [see Eq. (9)].

The geometrical constraint curves (parabolic like) calculated from Eq. (1) are overlaid on the same plot for corresponding interaction lengths. The allowed operation regions, indicated by broad dark lines, are those above the parabolic curves. It is evident from Fig. 5 that for $2l > 340$ μm, the prism always clips the input laser beam for the 0.7 GeV/m structure because the contour curve and the parabolic curve no longer intercept. Also, from the same plot, a larger θ and a smaller w_0, which produce larger plane wave phase and Guoy phase shift, are allowed when $2l$ is smaller because phase coherence is easier to maintain over a shorter distance.

Although a certain acceleration gradient may be achieved by applying many different combinations of θ and w_0, different (θ , w_0) pairs give different electron beam characteristics after acceleration. Energy spread and emittance are two important parameters for an electron beam. Because of the time and space variation of the laser field, electrons injected at a different instant and location acquire different transverse momenta and longitudinal momenta. Loosely speaking, energy spread is the rms electron energy divided by the electron mean energy, and emittance is the area occupied by the electrons in the angle and position space (phase space). A good electron beam should have a small energy spread and small emittance. Both quantities, energy spread and emittance, increase with the increase of field variation in space and in time. Ideally, one would like to have a large spot size and a small crossing angle such that the laser fields have less spatial variation. A large laser waist size also allows increased laser power within the laser damage fluence and thus to obtain more electron current for a fixed power conversion efficiency. Figure 5 shows that a short interaction length increases the allowed range of θ and w_0, but moves θ to a larger value and w_0 to a smaller value.

With current submicrometer lithographic technology, a device with a 50 μm feature size may give an ~ 10 mrad angle error in fabrication. We investigate in the following the impact of the fabrication error on the proposed accelerator structure.

An allowed region for θ and w_0 means that the system can be less sensitive to misalignment or fabrication errors. Figure 6 plots acceleration gradient vs. crossing angle for various laser spot sizes for $2l$ = 300 μm. Only those data points complying with the coupling condition in Eq. (1) are plotted. The gradient variation can be less than 5% even though the variation in θ is on the order of 10 mrads and the variation in w_0 is on the order of a micrometer, as the dashed box indicates. However, in making the above statements, we assume that the fabrication error influences both laser beams symmetrically and the perfect phase cancellation still applies. In practice, active feedback control would be needed to assure the phase cancellation.

3.4 Multistage Accelerator Structure

As discussed previously, the 0.7 GeV/m design (point A in Fig. 5) gives 0.24 MeV energy gain per accelerator microstage with a stage length of 334 μm. To achieve 1 TeV energy level, the accelerator would consist of a few million microstages. Since each

microstage consumes 0.2 GW of laser power, a single 0.1 TW laser source can illuminate 500 microstages in a distance of 16.7 cm, giving 118 MeV energy gain in such a *macrostage*. In the future, the 10,000 accelerator macrostages in the 1 TeV electron accelerator would be isolated from ground motion and stabilized within submicrometer accuracy. The 4 km × 4 km laser interferometer used for the Laser Interferometer Gravitational-wave Observatory (LIGO)[25] project has a similar requirement. The vibration isolation technology[26] for LIGO can be applied to the isolation and adjustment of the structure to the subnanometer dimensions required.

The optical phase and group velocity timing of each microstage also needs to be precisely controlled. Figure 7 shows the schematic of a multistage accelerator that can be integrated on a silicon wafer using current lithographic technology for mass production. The dimensions are consistent with the 0.7 GeV/m design discussed previously (point A in Fig. 5), namely, a laser waist = 17 μm, a stage length $2l + 2w$ = 334 μm, and a wavelength = 1 μm. In Fig. 7, we assume that a plane wave is incident on each focusing lens and thus a nominal 7 mm × 34 μm elliptical beam profile from a single laser source can drive 20 stages simultaneously. A dielectric channel of 4 μm diameter is assumed for transmitting electrons. The laser power transmitted by this channel is less than 1% of the incident power. The phase of laser fields is controlled by electro-optic phase controllers and the group velocity delay is controlled with slabs of dielectric. If necessary, microactuators or micromotors can be integrated into the same wafer in a batch process. These active controls will be addressed in more detail in Sec. 4.

4. Computer Simulations

Ideally, high energy physicists would like to have a monochromatic energy beam and a highly collimated or a tightly focused electron beam, but not a single energetic electron. The ensemble behavior of many electrons in a laser-driven accelerator needs to be studied statistically in computer simulation. Since electrons react to both electric and magnetic fields, all the vector fields of a Gaussian beam in Eqs. (2a)--(2e) ought to be taken into account. The paraxial approximation is valid for our design parameters (see Fig. 5) and is adopted in our computer simulations. The field profile of the crossed Gaussian beams is very similar to that of a guided wave; namely, it is a standing wave in

x and a traveling wave in z. Furthermore, the transverse electric field in x is an odd function with respect to the coordinate x, and its phase is delayed by 90° with respect to the longitudinal electric field. Physically, the off-axis electrons in the first 90° acceleration cycle experience a defocusing force, and those in the second 90° acceleration cycle experience a focusing force. As a result, electrons in the first 90° acceleration cycle may be detrapped in the subsequent accelerator stages. To show the laser-induced focusing and defocusing, we carried out particle simulation on a computer.

At the entrance of the accelerator, we assume approximately 3000 1 GeV electrons uniformly distributed inside a spatial cylinder with a half-wavelength length (0.5 μm) and a 2 μm diameter. For GeV electron beams, it has been demonstrated that the transverse beam size can be as small as 75 nm.[27] The field disturbance due to the 4-μm electron channel is ignored in the simulation. We also assume zero energy spread, zero emittance at the entrance.

4.1 Energy Gain and Energy Spread

Figure 8 shows the electron energy gain vs. time at the exit of one microstage. The time window corresponds to one half optical cycle. The system parameters are θ = 43 mrad, w_0 = 17 μm, interaction length $2l$ = 300 μm (point A in Fig. 5), wavelength = 1 μm, and power for each of the two crossed-laser beams = 0.1 GW (Eq. 8). It is evident from Fig. 8 that the highest energy gain of 0.24 MeV is obtained from the simulation. With an interaction length of $2l$ = 300 μm and a drift space of $2w \approx$ 34 μm, the energy gain gives an average acceleration gradient of 0.7 GeV/m that is consistent with the analytical formulas [Eqs. (4) and (9)]. The electron energy spread in the half optical cycle is attributable to the time-varying nature of the laser fields and the spatial variation of the Gaussian profile.

Suppose electrons in the central 10% of the half optical cycle (indicated by dashed lines in Fig. 8) are trapped in the down-stream acceleration; within this 10% time window, the rms energy spread, $\delta\gamma/\Delta\gamma$, referenced to the single-stage energy gain $\Delta\gamma$, is calculated to be 1%. This amount of energy spread is predominantly introduced by the spatial variation of the Gaussian profile over the 2 μm beam diameter. One can estimate the resulting energy spread after many stages as follows. Since the energy gain is linearly

proportional to the laser field, $\delta\gamma$ and $\Delta\gamma$ in the subsequent stages remain the same as those in the first stage. So the resulting energy spread after N acceleration stages is

$$\frac{\Delta E}{E} = \frac{\delta\gamma_i + N \times \delta\gamma}{\gamma_i + N \times \Delta\gamma}, \tag{10}$$

where γ_i is the initial electron energy, and $\delta\gamma_i / \gamma_i$ is the energy spread at the entrance of the first microstage. For a TeV multistage accelerator, N is on the order of a million, and the final energy spread in (10) converges to

$$\frac{\Delta E}{E} \approx \frac{\delta\gamma}{\Delta\gamma}, \tag{11}$$

which equals the energy spread referenced to the energy gain per stage. With the design parameters of Fig. 8, the final energy spread after a million acceleration stages can therefore meet the 1% criterion required by most experiments.

4.2 Emittance and Multistage Trajectory Stability

Figures 9(a) and 9(b), plotted on the same scales, are the electron distributions in the displacement and angle (*x-xp* and *y-yp*) phase planes at the exit of the first microstage. The electrons in the second and the fourth quadrants (labeled "+") propagate with convergent angles, and those in the first and third quadrants (labeled "–") propagate with divergent angles for the reason stated above. The area occupied by the electrons in the *y-yp* plane is approximately one-tenth of that in the *x-xp* plane, because electrons experience a second-order force in *y*. The small electron angle in both transverse phase planes, on the order of microradians, is a consequence of the small crossing angle and the large optical mode size compared to the electron beam size; the former results in little wavelength modulation in the *x* direction, and the latter gives almost zero transverse fields across the electron beam size. The normalized rms emittances in the two transverse dimensions, for the electrons in the 10% of the half optical cycle, are $\varepsilon_{x,n} = 1.3 \times 10^{-4}$ π-mm-mrad and $\varepsilon_{y,n} = 2.1 \times 10^{-5}$ π-mm-mrad, which are about four orders of magnitude lower than those for a conventional RF accelerator. Small emittance, which means high brightness, opens the potential for performing experiments with a lower current.

The trajectory stability of electrons in successive stages is estimated as follows. The accelerator stages can be viewed as a lens array in which identical lenses are

arranged along z with a periodicity of L_μ. If the optical phase seen by the electrons remains the same in all accelerator stages, the electrons in the first 90^c acceleration phase see a focusing lens array, whereas those in the second 90^c acceleration phase see a defocusing lens array. Assuming the thin lens approximation and a drift distance of L_μ between two adjacent lenses, the transverse coordinate x_n, and angle xp_n, of an electron at the exit of the nth acceleration stage can be expressed in terms of its initial coordinate x_1, and its initial angle xp_1 using:

$$\begin{bmatrix} x_n \\ xp_n \end{bmatrix} = M^n \begin{bmatrix} x_1 \\ xp_1 \end{bmatrix}, \tag{12}$$

where $M = \begin{bmatrix} 1 & L_\mu \\ 0 & 1 \end{bmatrix} \begin{bmatrix} 1 & 0 \\ -1/f & 1 \end{bmatrix} = \begin{bmatrix} 1 & L_\mu \\ -1/f & 1 - L_\mu / f \end{bmatrix}$. The focal length, f, is positive for a focusing lens (seen by the electrons is the second 90° acceleration phase) and negative for a defocusing lens (seen by the electrons is the first 90° acceleration phase). The criterion for a stable electron trajectory[24] is

$$\left| 1 - \frac{L_\mu}{2f} \right| \le 1 \ . \tag{13}$$

Equation (13) is satisfied for a positive focal length. In other words, those electrons in the second 90° acceleration phase perform stable oscillatory motions in the accelerator stages. It can be shown that the maximum amplitude in x of the oscillatory trajectory is given by

$$x_{\max} = \sqrt{\frac{4f}{4f - L_\mu}(x_1^2 + L_\mu x_1 xp_1 + L_\mu f xp_1^2)} \ . \tag{14}$$

Using the electrons in Fig. 9(a) as the injection condition for the subsequent stages: L_μ = 334 μm, $x_1 \approx 1$ μm, $xp_1 \approx 1$ μrad, and $fxp_1 \approx x_1 \approx 1$ μm, we found that $x_{\max} \approx$ 1 μm, which is well within the 4 μm diameter aperture of the dielectric accelerator structure. For the electrons in the first 90° acceleration phase, a similar calculation shows that the electrons with initial coordinates $|x_1| > 15$ nm strike accelerator structure within the first 10,000 microstages.

4.3 Phase Cancellation and Group Velocity Control

The focusing and the phase canceling of the two crossed-laser beams can be precisely controlled by PZT or electro-optic (EO) phase controllers. For example, a PZT can change the optical path with a sub-Angstrom step size, which is ~ 0.1 mrad on the optical phase for a 1 μm wavelength. The PZT or EO controllers can be integrated onto the accelerator substrate with modern lithographic technology. If the two laser beams are misaligned transversely by 1 A, the net effect is similar to sending an electron beam off axis by 1 A. As can be seen in Fig. 9, the deflection angle of the electron acquired from the 1 A focusing error is on the order of 10^{-10} radian per stage. With this minute amount of side-kick per accelerator stage and an equal probability of random errors in both transverse directions, the electron trajectory stability should not be a problem for our accelerator structure.

5. Laser Requirements and Luminosity

The advance in high peak power, high efficiency, short pulse solid-state lasers has been revolutionary. High power, long life, compact diode lasers, which efficiently provide pump power near the absorption band of solid-state materials, have replaced the low efficiency, short life, bulky flash lamps for pumping solid-state lasers.[28] Several short-pulse, high peak power laser sources, such as Ti:Sapphire, Nd:Glass, Yb:YAG, Nd:YLF, and Nd:YAG lasers, are potential candidates for laser acceleration. The pulse length range for these lasers is shown in Fig. 1(b). A Ti:Sapphire laser, usually pumped by an Ar ion laser due to the lack of high power diode lasers in the Ti:Sapphire absorption band at ~ 550 nm, can generate femtosecond pulses and thus a higher acceleration gradient [see Fig. 1(b)]. However, its electrical efficiency may not be as good as a diode-pumped Nd:YLF or Yb:YAG laser (which can also generate picosecond or subpicosecond pulses). Figure 1(b) provides a scaling law, $E_g \propto \tau_p^{-0.44}$, for the acceleration gradient for τ_p on the order of a few picoseconds or less. For example, if one employs a laser with 1 psec pulses and adopts the 0.7 GeV/m structure designed for 100 fsec lasers, the acceleration

gradient drops to 0.25 GeV/m. With the constant rate of the advancement in solid-state lasers, we believe a solid state laser that meets the peak power, efficiency, pulse length, and repetition rate required for a laser accelerator will appear within the decade.

The optical pulse structure for driving the accelerator is illustrated in Fig. 10. The 50 nsec macropulse is generated by the Q-switch pump laser of the regenerative amplifier. The repetition rate for the Q-switch laser can be a few tens of kilo-Hertz. Each macropulse contains ~ 10 micropulses from the mode-locked master oscillator, and a micropulse of 100 fsec length (FWHM) contains ~ 30 optical cycles at a 1 μm wavelength. The separation of adjacent mode-locked pulses (micropulses), which is typically on the order of a few nanoseconds, is determined by the intracavity length of the master oscillator.

Phase coherence in successive accelerator stages is necessary for continuous acceleration. Precise phase locking of individual lasers is required. Regenerative amplifiers after the master oscillators add complexity to this issue. Locking the phase between two CW lasers has been demonstrated in the past,[29] but locking the phase between two mode-locked lasers before and after regenerative amplifiers needs to be demonstrated. The principle of a mode-locked laser is essentially the same as that of a CW laser except that there is a fixed phase relationship among the longitudinal modes in a mode-locked laser. We believe locking the phase between two mode-locked lasers should be achievable without undue difficulty.

Since each microstage consumes 0.2 GW laser peak power, a single 0.1 TW laser source can illuminate 500 microstages in a distance of 16.7 cm, giving 118 MeV energy gain in such a *macrostage*.

Luminosity is critical for the application of the accelerator to high energy physics experiments. Luminosity is defined as

$$L(\mathrm{cm}^{-2}\cdot\mathrm{sec}^{-1}) \equiv \frac{mnfN^2}{\sigma_x\sigma_y}, \tag{15}$$

where m is the number of optical cycles per optical micropulse, n is the number of micropulses in a macropulse, f is the laser repetition rate for the macropulse, and σ_x and σ_y are the two transverse beam sizes. The minimum luminosity requirement[30] for next

generation high energy physics is in the range of 10^{31} cm$^{-2} \cdot$ sec^{-1} ~ 10^{34} cm$^{-2} \cdot$ sec^{-1}, depending on the type of investigation to be performed.

Electrons radiate when they traverse the dielectric-based accelerator structure. The coherent Cherenkov or transition radiation loss essentially limits the maximum number of electrons that can be accelerated in one optical cycle. To first order, the radiation loss per electron per accelerator stage is approximately[31]

$$\Delta W_l = \frac{Ne^2}{\lambda}, \qquad \text{(CGS units)} \qquad (16)$$

where N is the number of electrons in one optical cycle and λ = 1 μm is assumed to be equal to the laser wavelength. For $\Delta W_l / \Delta W \le 10\%$ per accelerator stage, the maximum N is 1.6×10^7 per optical cycle. With m = 30 for 100 fsec laser pulses, n = 10, f = 33 kHz for current mode-locked lasers, σ_x = 160 nm and σ_y = 1.6 nm scaled from the Next Linear Collider,[32] the luminosity for our accelerator structure is ~ 10^{33} cm$^{-2} \cdot$ sec^{-1}. The corresponding required average laser power (with an assumed 10% power conversion efficiency from the laser to the electron beam) is 180 kW/m or 180 MW/km. Assuming that the dielectric substrate is 5 cm wide and the laser deposits 10% of its power to the substrate, the power dissipation needed for the substrate is 36 W/cm^2. Note that the luminosity could be enhanced further or the average laser power could be reduced at the same luminosity, since the electron beam emittance of a laser accelerator may be much better than that of an RF accelerator.

6. One-Dimensional Laser Focusing

In the previous sections, we analyzed the performance of our laser-driven accelerator structure by using two crossed laser beams symmetrically focused in the two transverse directions, x and y. However, the optical elements in the accelerator structure proposed

in Fig. 7 can be constant in y. In practice, fabricating a cylindrical lens array by using chemical or plasma etching is less complicated than fabricating a spherical lens array. In addition, cylindrical (one-dimensional) focusing increases the optical mode volume and therefore the coupling efficiency; spreading the electrons in one transverse direction also helps to reduce the beamstrahlung at the final focusing stage. In the following, we investigate and compare the performance of a one-dimensional accelerator structure with respect to the two-dimensional structure.

6.1 Acceleration Fields and Phases

With a constant field profile in y, the electrical field in x' for a fundamental Gaussian mode is[24]

$$E_{x'} = \left(\frac{2}{\pi}\right)^{1/4} \sqrt{\frac{2\eta}{w(z')}\frac{dP}{dy}} \exp[-jkz' + j\frac{1}{2}\Phi(z') - jk\frac{x^2}{2R(z')}] \times \exp[-\frac{x'^2}{w^2(z')}], \qquad (17)$$

where $\frac{dP}{dy}$ is the optical power per unit length in y and w is the laser beam radius in x. Note that only one half of the Guoy phase appears in Eq. (17) for one-dimensional focusing because the wave front parallel to y does not contribute any phase other than the plane-wave phase in the z' direction.

The electrical field vector in the z' can be calculated from

$$E_{z'} = -\frac{j}{k}\nabla_{x'} \cdot E_{x'}(x', z'), \qquad (18)$$

which gives

$$E_{z'} = E_{x'} \cdot [\frac{-x'}{R(z')} + 2j\frac{x'}{kw^2(z')}]. \qquad (19)$$

With the coordinate transformation in Eqs. (3a)--(3b), the resulting axial acceleration field with a small crossing angle θ is

$$E_z = -2\left(\frac{2}{\pi}\right)^{1/4} \sqrt{\frac{2\eta}{w_0}\frac{dP}{dy}} \cdot \theta \cdot \frac{\exp\left(\frac{-\xi^2\theta^2}{1+\xi^2}\right)}{(1+\xi^2)^{3/4}} \cdot \cos\left(\frac{\xi\theta^2}{1+\xi^2} + 1.5\tan^{-1}\xi\right). \qquad (20)$$

As previously noted, the maximum acceleration gradient is limited by the laser-induced damage on the optical components. For the one-dimensional focusing case, the

maximum power per unit length in y, $\left(\frac{dP}{dy}\right)_{\max}$, can be related to the damage threshold intensity $I_{\max}$ by

$$\left(\frac{dP}{dy}\right)_{\max} = I_{\max}\sqrt{\frac{\pi}{2}}w(l)\,, \tag{21}$$

where $z = l$ is the location of the HR mirror.

Substituting Eq. (21) into Eq. (20), one obtains the following on-axis acceleration field:

$$E_z = -2\sqrt{2\eta I_{\max}}\cdot\theta\cdot\frac{(1+\xi^2)^{1/4}}{(1+\xi^2)^{3/4}}\cdot\exp\left(\frac{-\xi^2\theta^2}{1+\xi^2}\right)\cdot\cos\left(\frac{\xi\theta^2}{1+\xi^2}+1.5\tan^{-1}\xi\right). \tag{22}$$

The corresponding on-axis acceleration field for the two-dimensional focusing case can be calculated from Eqs. (4a) and (8), yielding

$$E_z = -2\sqrt{2\eta I_{\max}}\cdot\theta\cdot\frac{(1+\xi^2)^{1/2}}{(1+\xi^2)}\cdot\exp\left(\frac{-\xi^2\theta^2}{1+\xi^2}\right)\cdot\cos\left(\frac{\xi\theta^2}{1+\xi^2}+2\tan^{-1}\xi\right). \tag{23}$$

It is worth noting that the phase of the one-dimensional focusing varies slower in z due to the removal of the 0.5 Guoy phase from the y direction. However, at the focus, the axial acceleration field of the two-dimensional focusing is stronger by a factor of $(1+\xi^2)^{1/4}$. Figure 11 shows the normalized axial acceleration fields vs. z for the two types of focusing at $\xi = 0.46$ and $\theta = 1.37$, where the two-dimensional focusing obtains the maximum energy gain per stage [see Eq. (7)]. It is seen that the axial field for the one-dimensional focusing is indeed slightly weaker at the focus but decreases more slowly due to the weaker dependence on the Guoy phase. As a result, the axial field for the two-dimensional focusing reduces to zero at $|\xi| = 0.46$, corresponding to a π phase shift, while for the one-dimensional focusing, it remains nonzero. The energy gain per stage for both cases is the area under the two curves. It can be seen that the one-dimensional focusing has a higher energy gain per stage under the same damage fluence at $\xi = 0.46$.

6.2 Average Acceleration Gradient

The average acceleration gradient is the energy gain per accelerator stage divided by the repeat distance L_μ. We illustrate in Fig. 12 the 0.71 GeV/m gradient contours in the θ-w_0 space for an interaction length of $2l$ = 340 μm for the one-dimensional and two-dimensional focusing. The one-dimensional focusing curve is obtained by numerically integrating the axial field over z and dividing the result by L_μ, whereas the two-dimensional curve is calculated from Eq. (9). The geometrical coupling condition Eq. (1) is overlaid in the same plot. In Fig. 12, only the one-dimensional focusing curve intercepts the geometrical coupling condition; in other words, the two-dimensional focusing cannot achieve the 0.71 GeV/m average gradient with an interaction distance of 340 μm per stage. It is evident from the figure that the one-dimensional focusing curve still provides a range of (θ, w_0) to achieve the 0.71 GeV/m gradient. For example, if point B in Fig. 12 is chosen to be the operation point for the one-dimensional focusing, 0.71 GeV/m is obtained with a crossing angle θ = 50 mrad, a laser waist size w_0 = 25 μm, a repeat distance L_μ = 390 μm, and the single-stage energy gain = 280 KeV. Compared to the previous two-dimensional focusing design (point A in Fig. 5), the one-dimensional focusing design reduces the number of the total microstages by 0.5 million over 1 km while providing the same final electron energy.

6.3 Fabrication Techniques

Since the invention of the semiconductor amplifier in 1948 by Brattain, Bardeen, and Shockley, semiconductor-related applications have become perhaps the most notable industry in the 20th century. Along with the growth of the semiconductor industry, microfabrication techniques have been advanced dramatically to provide high precision and low-cost solid-state devices. In this section, we will delineate the feasibility of constructing our accelerator structure by using current microfabrication technology.

The fabrication of the proposed accelerator structure is essentially a combination of integrated optics and lithographic techniques. Conventional micromachining may have difficulties in cutting and polishing components with a 50 ~ 500 μm feature size. Although the etching depth of a typical semiconductor component is on the order of a micron, a depth of a few hundred microns, which is suitable for cylindrical focusing, appears to be feasible with current lithographic technology. Figure 13 illustrates quartz

blocks with a base size of 100 μm × 100 μm and a height of 300 μm, which are etched on a host quartz substrate. The surface smoothness is about 2% of the 1 μm wavelength, the center-to-center position accuracy is ~ 0.1 μm, and the vertical slop is approximately 10 mrad.

Components of different materials such as the EO phase controller and PZT can be fabricated separately and then implanted into the same host substrate. For example, the so-called fluidic self-assembly technique[33] is capable of assembling microcomponents with specific binding features to the host substrate in a large quantity. This assembly technique derives the concept from the protein binding mechanism where protein molecules with specific feature shapes bind to biological sites that fit with the feature shapes. Microcomponents are first fabricated from their sacrificial substrate and then carried by an inert fluid to the host substrate. The binding sites on the host substrate differentiate the microcomponents according to the specific binding keys on the microcomponents. This technique is suitable for assembling a large amount of microcomponents.

PZT controllers, with a step size of an Angstrom per volt, can provide very precise positioning for the optical components. Microactuators or micromotors, with a step size of a submicron, can be useful for coarse adjustment. Figure 14 shows a 500 μm wide, 1000 μm high, 2 μm thick gold-coated mirror[34] for semiconductor laser applications. The position of the mirror can be controlled within 0.2 μm by a microactuator. To apply this mirror to our accelerator structure, a dielectric-coated surface will be used for the high-power lasers.

7. Summary

We have evaluated the energy gain, average acceleration gradient, and particle dynamics for the proposed dielectric-based, crossed-laser-beam electron linear accelerator structure under several engineering considerations such as laser-induced damage, the geometric beam coupling, fabrication techniques, laser requirements, laser focusing, and luminosity.

With laser parameters of λ = 1 μm, laser waist = 17 μm, laser power = 0.2 GW, crossing angle = 42 mrad, and 2 J/cm^2 damage fluence for an 100 fsec laser pulse, an average acceleration gradient of 0.7 GeV/m is achievable in the proposed multistage

accelerator structure. Optical components occupy approximately a 10% length in the electron acceleration direction. A phase slip less than π between the electrons and the laser fields is allowed in each accelerator microstage. The low-cost, high-precision modern lithographic technology can be employed to integrate hundreds of accelerator stages on a single silicon wafer which can be illuminated by a single laser source.

Using the beam diameters σ_x = 160 nm and σ_y = 1.6 nm, 33 kHz macropulse repetition rate, ten micropulses in one macropulse package, 100 fsec micropulse length, and an assumed 10% radiation loss, the beam luminosity is $10^{33}\ \mathrm{cm}^{-2} \cdot \mathrm{sec}^{-1}$ for the proposed design.

In our single-stage particle simulation, we injected 3000 1 GeV, zero emittance, zero energy spread electrons with a 2 μm beam diameter into the crossed-laser-beam accelerator structure. The electron energy spread in the central 10% of the half optical cycle converges to 1% after many stages. The emittance growth is negligible compared to that of an RF accelerator.

Our analysis for one-dimensional and two-dimensional laser focusing indicates that the optical mode, and therefore, the electron beam size, can be extended in one of the transverse dimensions without sacrificing the average acceleration gradient. The increase in the optical mode size is expected to increase the cavity shunt impedance and thus the coupling efficiency.

Recently, we have proposed experiments to verify the physics and the performance for the crossed-laser beam accelerator. The first goal for experimental work is to observe single-stage electron acceleration governed by our analysis; the second goal is to achieve multistage acceleration with controllability on phase coherence along successive stages. With the demise of the SSC project, there has been renewed interest in advanced accelerator concepts for building the next linear collider within a manageable cost and distance. Many groups such as LBNL, LLNL, UCLA, and NRL are working to explore possibilities both with theoretical studies and proposed experimental programs. We believe that in the foreseeable future, laser acceleration will play a significant role in high gradient electron acceleration.

Our future theoretical work includes the study of beam loading, wake field issues, and multistage particle simulations.

Acknowledgments

The authors appreciate valuable comments from S. Chattopadhyay, M. J. F. Digonnet, M. M. Fejer, C. Joshi, W. D. Kimura, R. H. Pantell, R. Ruth, A. Sessler, P. Sprangle, W. M. Tulloch, J. Wuetele, D. Zheng, and S. Zholents.

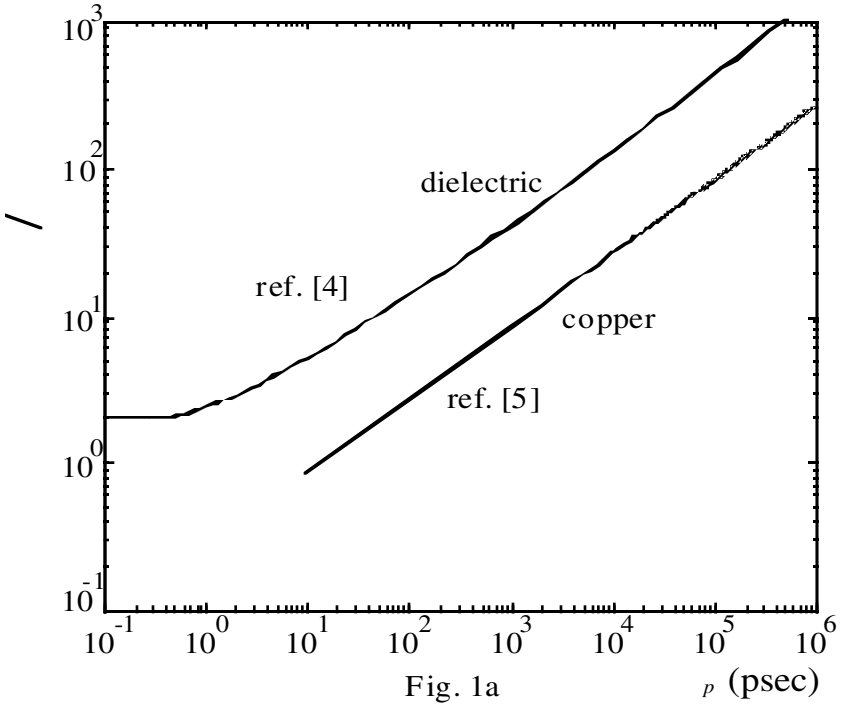

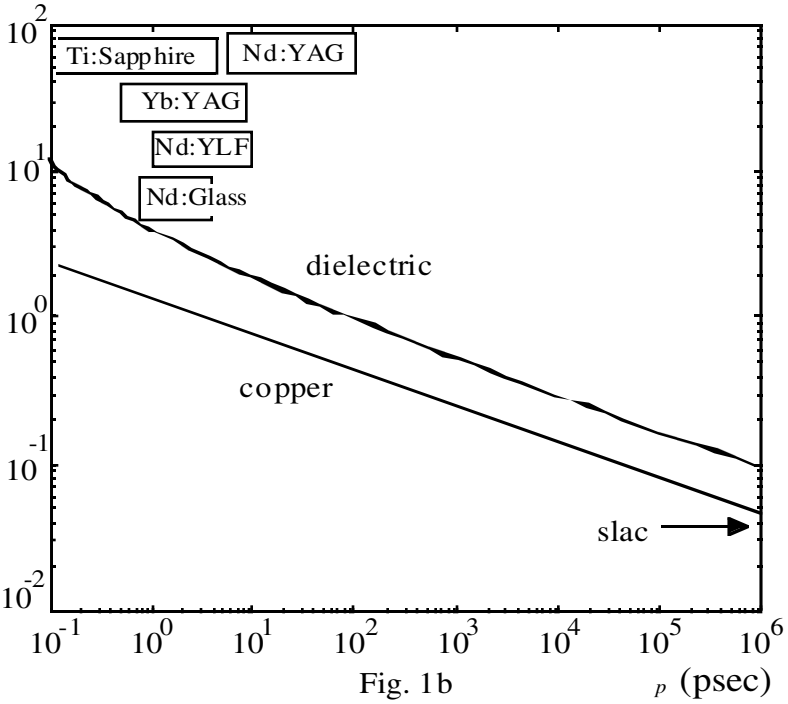

Figure 1: (a) Damage threshold fluence for a dielectric and copper vs. laser pulse length. Dielectric can sustain a fluence that is one order of magnitude higher than copper. (b) Surface field strength (the maximum acceleration gradient) at damage threshold. Laser sources that operate at the corresponding pulse lengths are indicated on the graph.

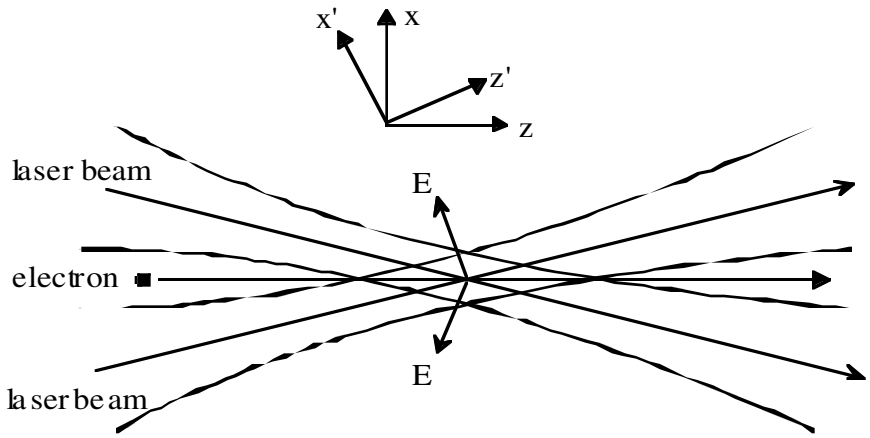

Figure 2a

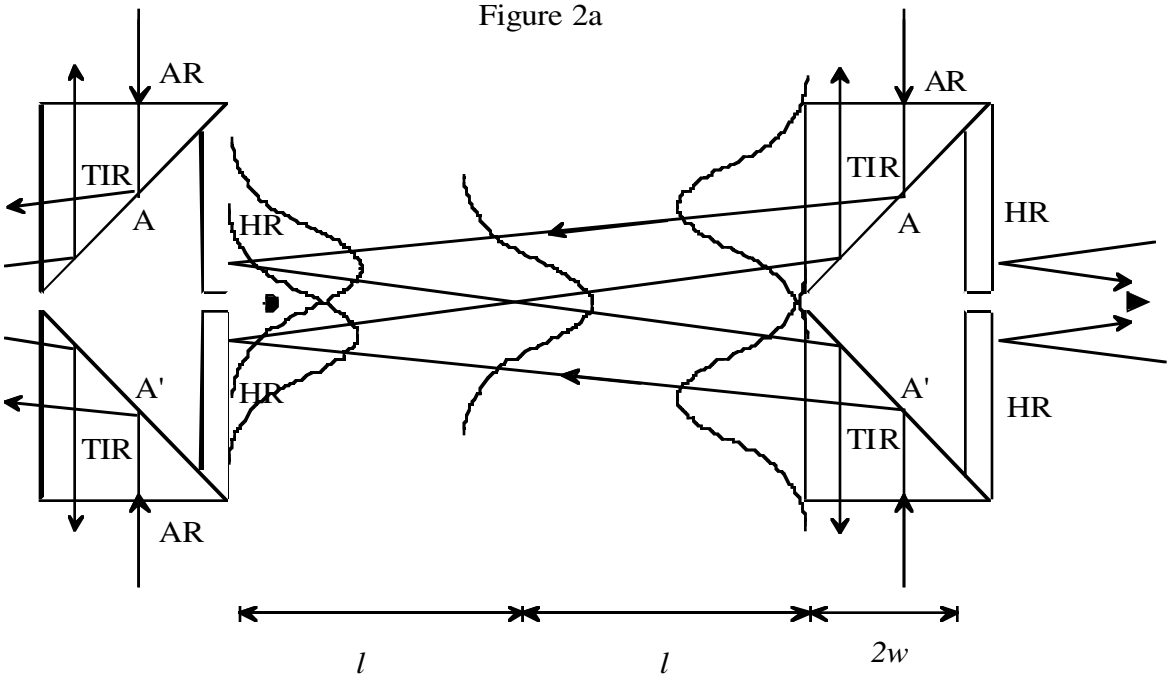

Figure 2b

Figure 2: (a) The schematic for a crossed-laser-beam accelerator. The electron traverses the focal zone at an angle θ with respect to each of the two beams. The two laser beams are phased such that the longitudinal fields add and the transverse fields cancel. (b) The back-coupled scheme for a single microstage. This scheme avoids clipping laser power at the coupling prisms. The drift space occupied by optical components for each microstage is approximately two laser spot sizes, $2w$.

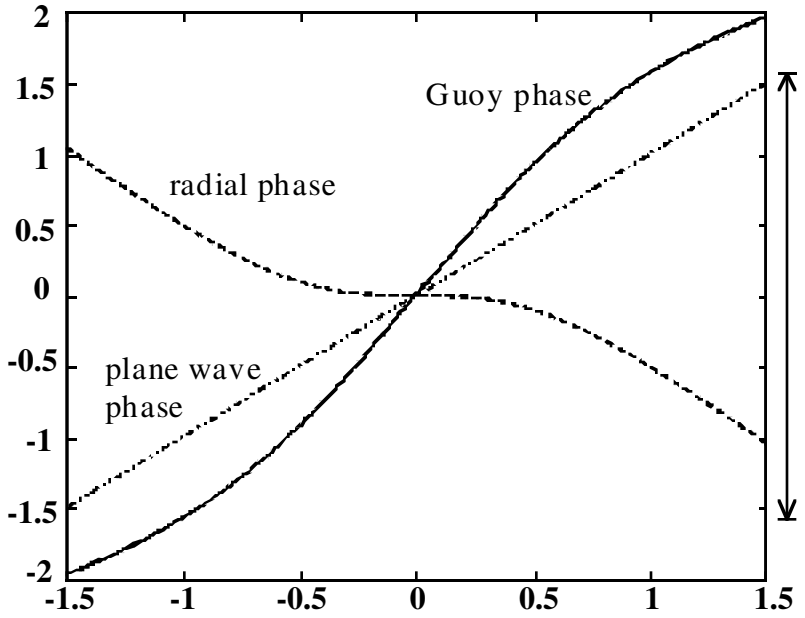

Fig. 3a

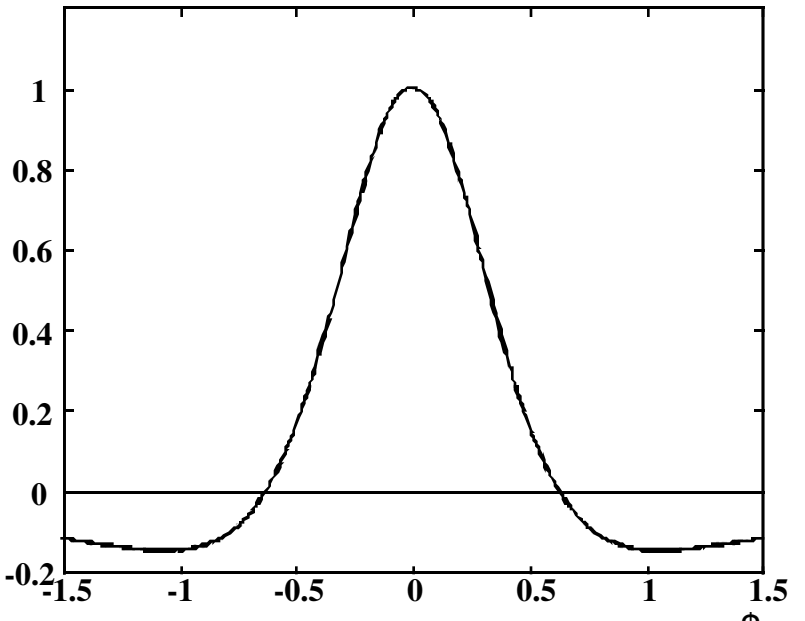

Fig. 3b

Figure 3: (a) Plane wave phase, Guoy phase, and radial phase for $\theta = 1$. The Guoy phase give a π shift from $-z_r$ to $+z_r$. (b) Normalized axial field along z. Field termination is necessary in ~ 1 Rayleigh length.

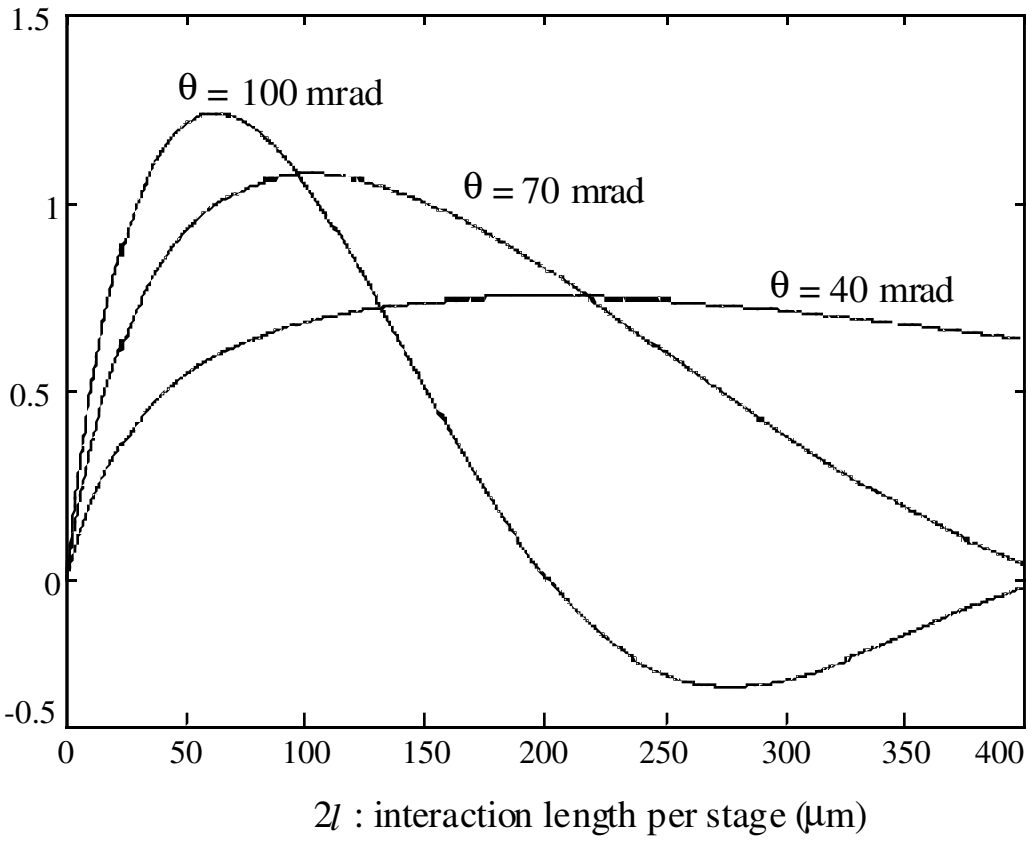

Figure 4: Average acceleration gradient vs. acceleration length for various crossing angles. Gradients exceeding 1 GeV/m are achieved for a device length of ~ 100 μm.

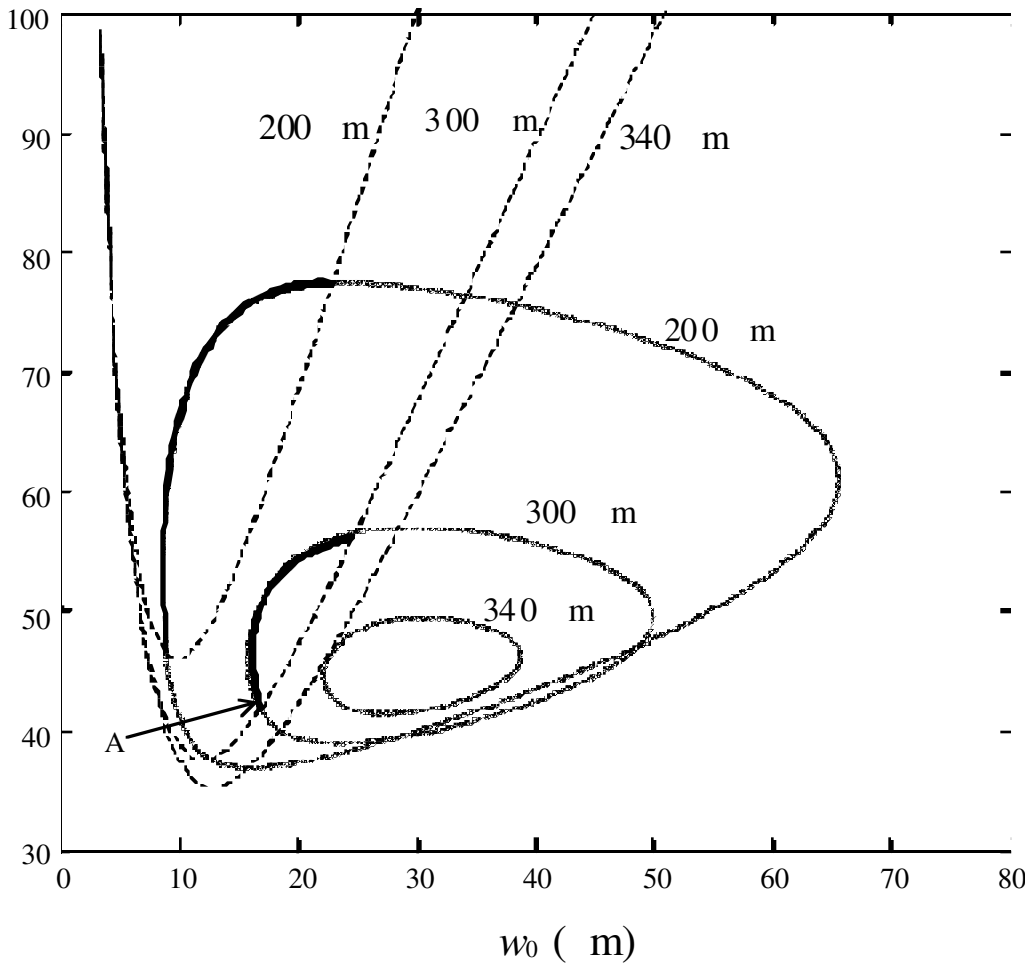

Figure 5: 0.7 GeV/m contours on the θ vs. w_0 plane for various interaction lengths, $2l$. The parabolic curves are calculated from Eq. (1) for the same $2l$. The allowed (θ, w_0) pairs are those on the contours and above the corresponding parabolic curves. Point A is to be discussed in simulations.

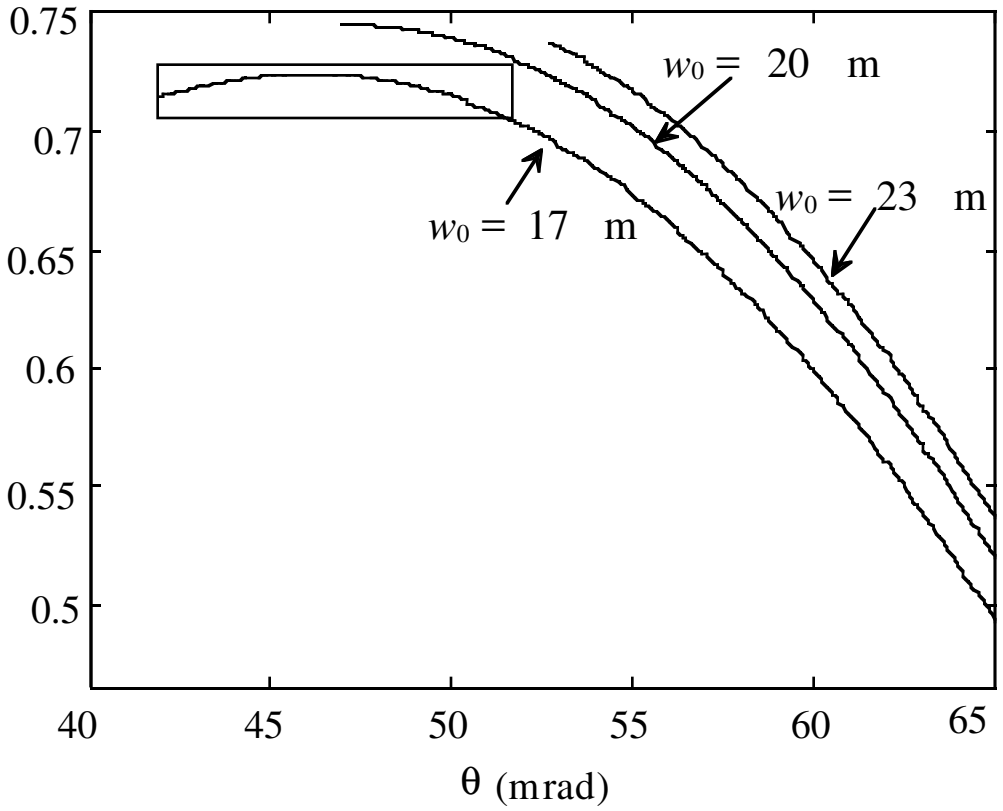

Figure 6: Acceleration gradients vs. crossing angles for various laser spot sizes for $2l$ = 300 μm. Only those data points complying with the coupling condition Eq. (1) are plotted. The gradient variation can be less than 5% even though the variation of θ is on the order of 10 mrads and the variation of w_0 is on the order of a micrometer as the dashed box indicates.

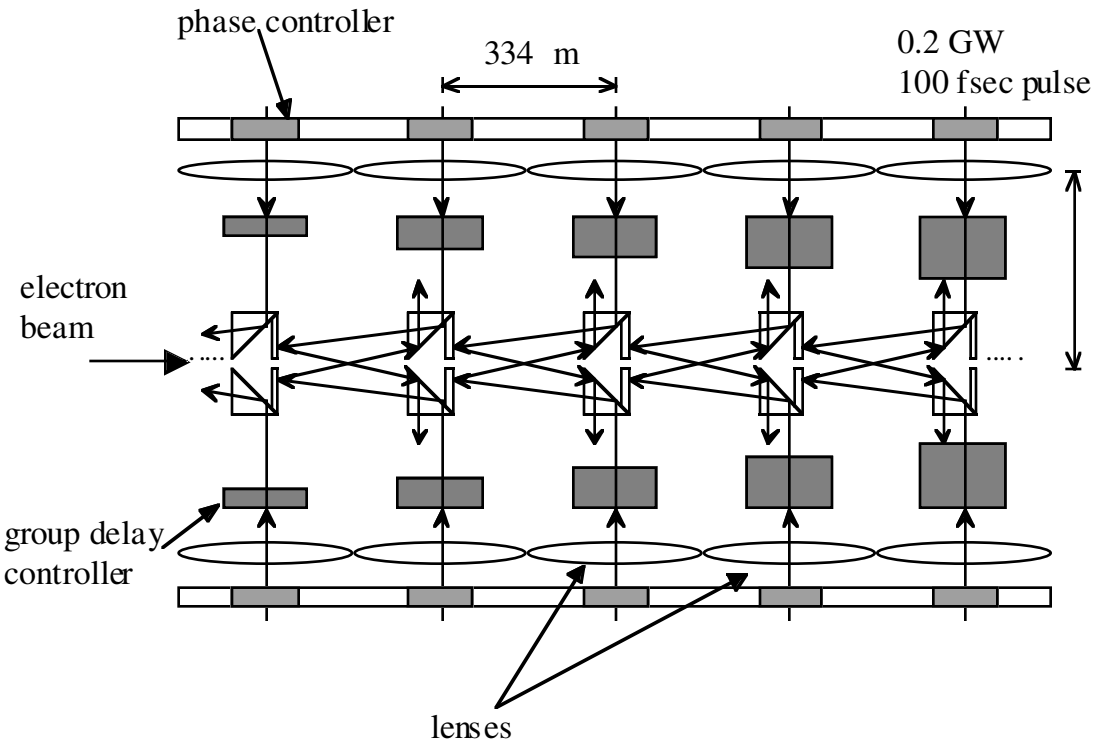

Figure 7: A multistage accelerator that can be integrated on a silicon wafer using lithographic technology. The dimensions are consistent with the 0.7 GeV/m design discussed previously (point A in Fig. 5).

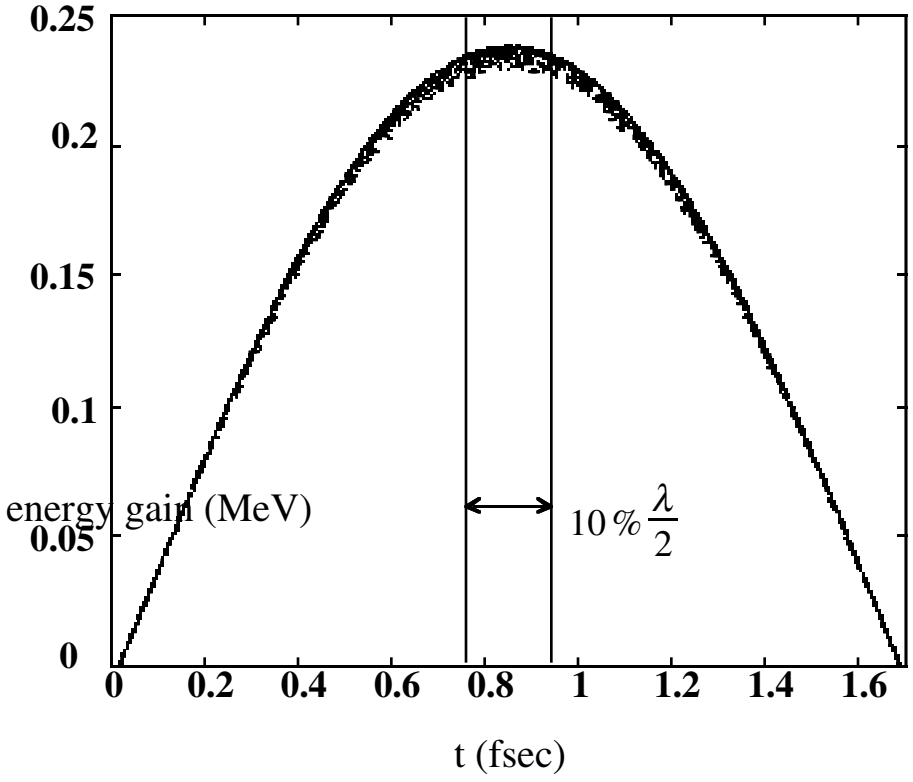

Figure 8: Electron energy gain at the exit of the first microstage. The energy spread referenced to the energy gain in the 10% of the half-optical cycle is 1.0%. With the design parameters of interaction length $2l = 300$ μm and drift space $2w \approx 34$ μm, the acceleration gradient is 0.7 GeV/m.

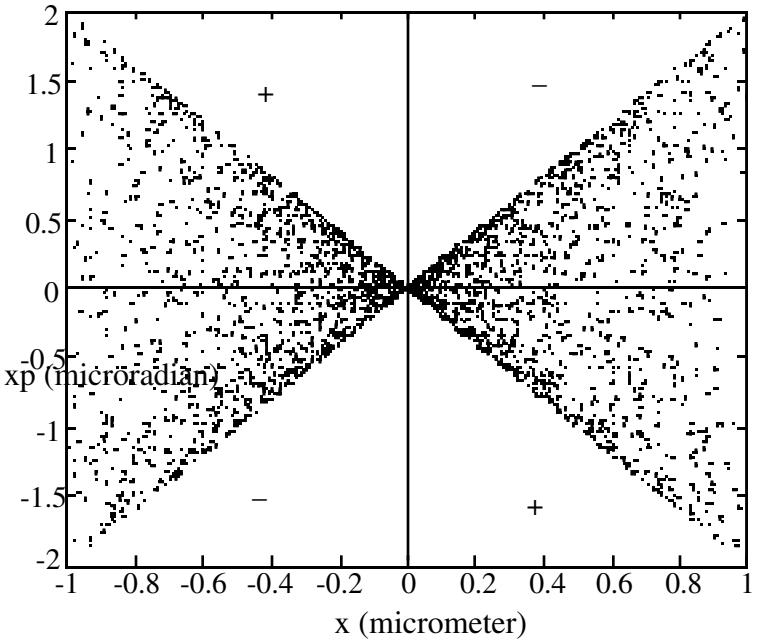

Figure 9a

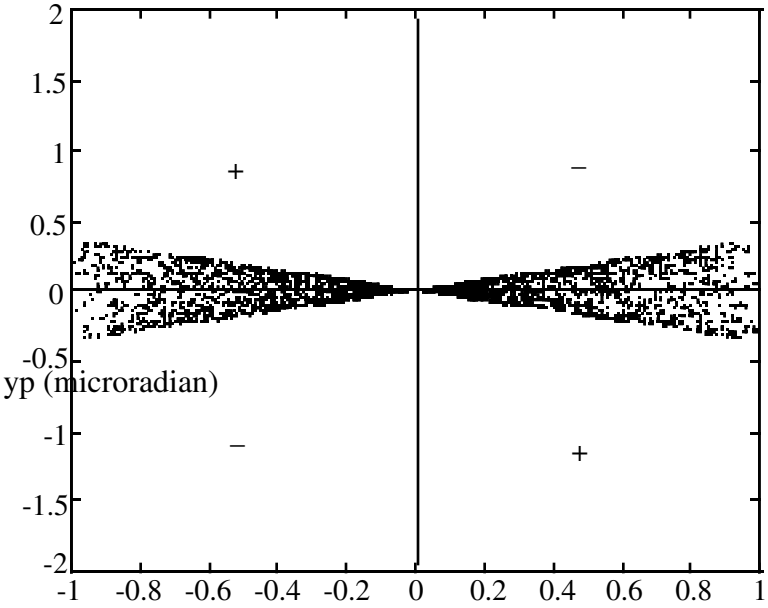

Figure 9b

Figure 9: Electron distributions in the (a) *x-xp* and (b) *y-yp* phase planes at the exit of the first microstage. Normalized rms emittances in the two transverse dimensions, including the electrons in the 10% half-optical cycle, are $\varepsilon_{x,n} = 1.3 \times 10^{-4}$ π -mm-mrad and $\varepsilon_{y,n} = 2.1 \times 10^{-5}$ π -mm-mrad.

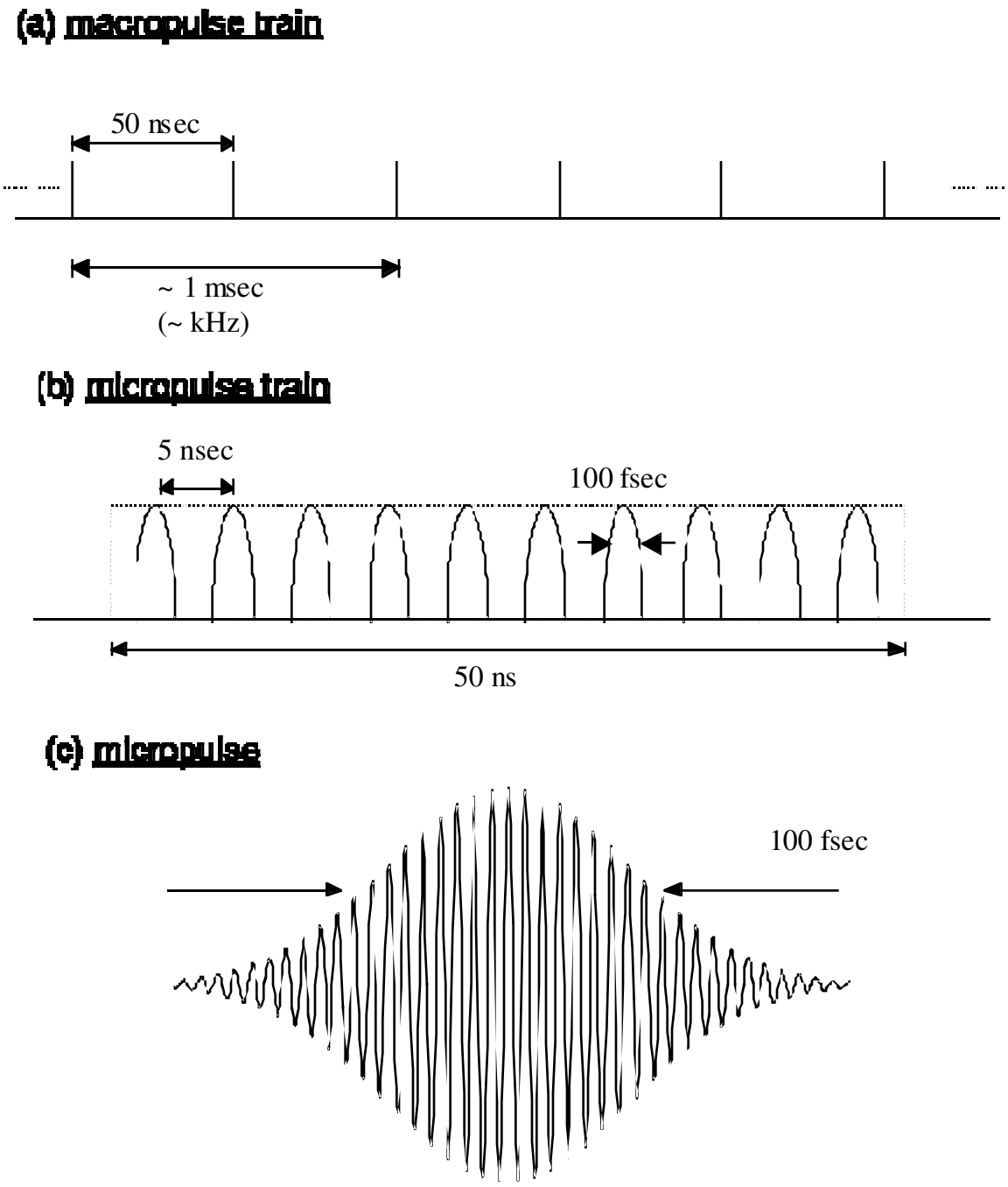

Figure 10: (a) Macropulse train generated by a Q-switch laser. The repetition rate can be a few tens of kilo-Hertz. (b) A macropulse consists of a few micropulses from the mode-locked master oscillator. (c) A 100 fsec micropulse consists of ~ 30 optical cycles for a 1 μm wavelength.

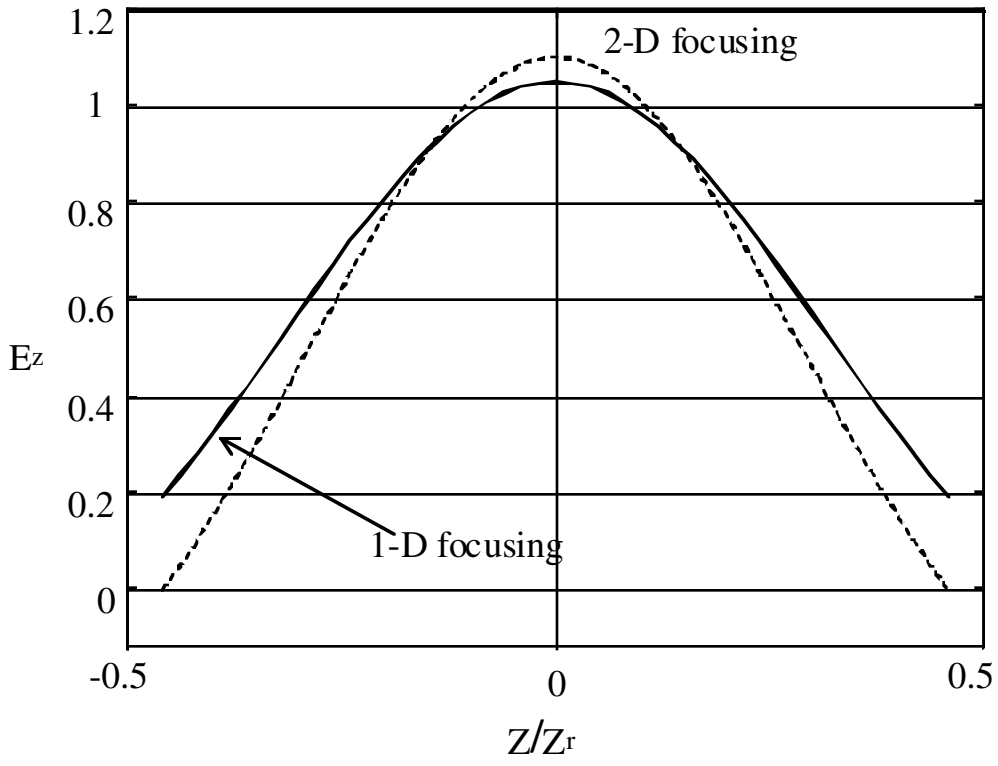

Figure 11: The normalized axial acceleration fields for the one-dimensional and two-dimensional focusing at $\hat{\rho} = 0.46$ and $\hat{\theta} = 1.37$. The curve for the one-dimensional focusing is weaker at the focus but decreases more slowly along z.

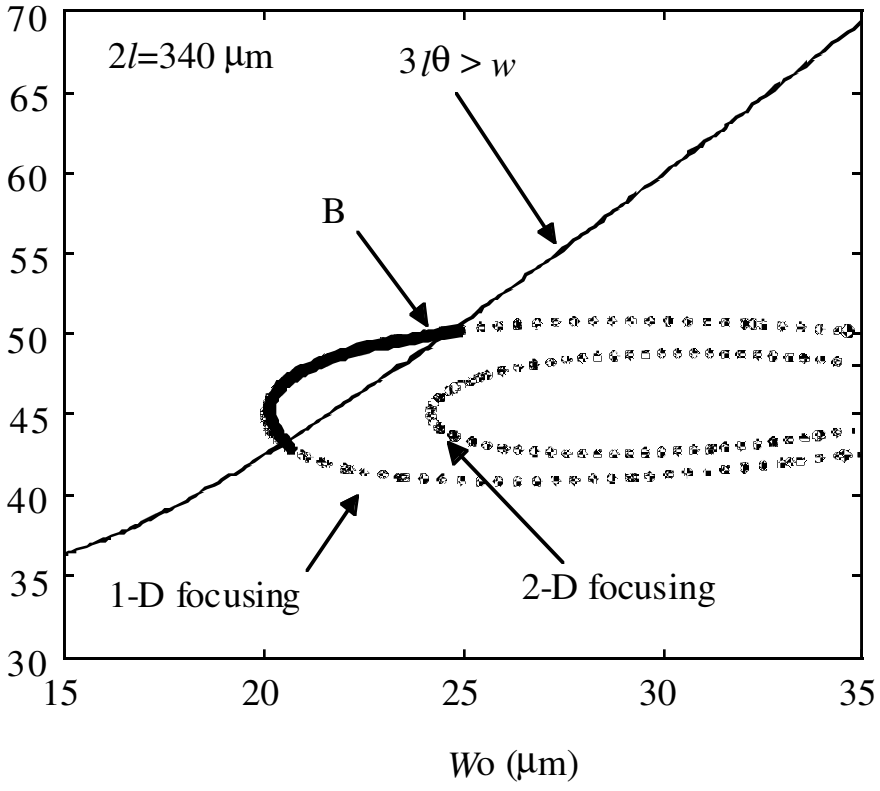

Figure 12: 0.71 GeV/m contours for the one-dimensional and two-dimensional focusing for $2l$ = 340 μm. No working (θ, w_0) pairs are obtained for the two-dimensional focusing. Point B for the one-dimensional focusing gives a 0.71 GeV/m average gradient with θ = 50 mrad, w_0 = 25 μm, L_μ = 390 μm, and single-stage energy gain = 280 keV.

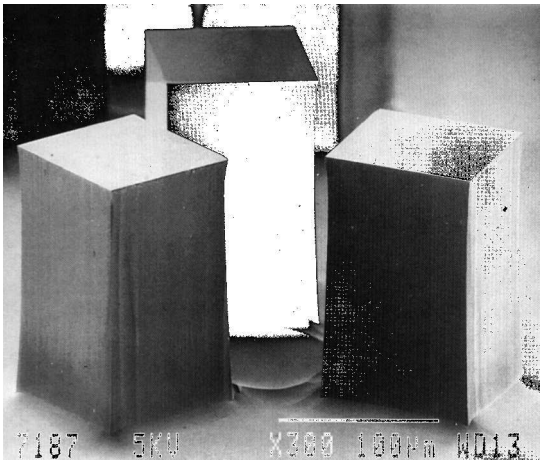

Figure 13: Three 100 µm × 100 µm × 300 µm dielectric blocks etched from a quartz substrate. The surface smoothness is about 2% of the 1 µm wavelength, the center-to-center position accuracy is ~ 0.1 µm, and the vertical slop is approximately 10 mrad. (Photo courtesy of Photonic Integration Research, Inc.)

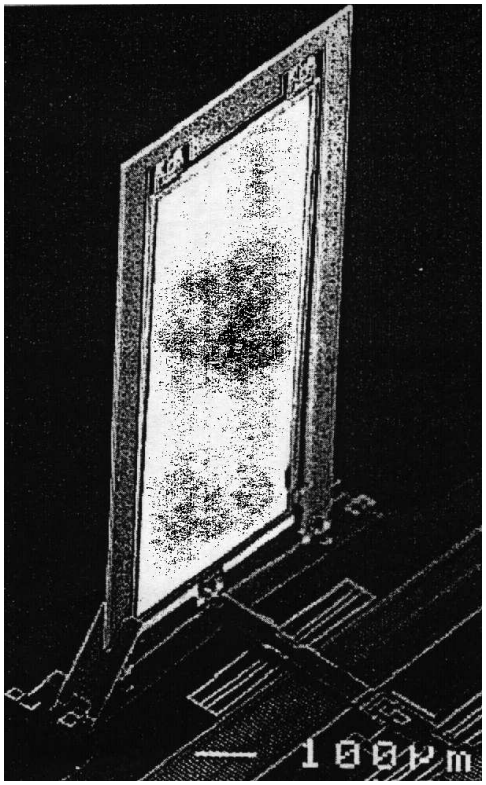

Figure 14: A 2 µm × 500 µm × 1000 µm gold-coated mirror driven by a microactuator with a 0.2 µm step size. (Photo courtesy of Meng-Hsiung Kiang.[34])

References

[1]E. Tanabe, Applied Surface Science, Vol. **76-77**, pp. 16-20 (March 1994).

[2]M. S. Livingston and J. P. Blewett, *Particle Accelerators* (McGraw-Hill, New York, 1962).

[3]R. L. Byer, Science, Vol. **239**, No. 4841, pp. 742-747 (February 1988).

[4]B. C. Stuart, M. D. Feit, A. M. Rubenchik, B. W. Shore, and M. D. Perry, Phys. Rev. Let., Vol. **74**, No.12, pp. 2248-2251 (March 1995).

[5]J. F. Figueira and S. J. Thomas, "Damage thresholds at metal surfaces for short pulse IR lasers," *IEEE J. Quan. Elect.* Vol. **QE-18**, No. 9, pp. 1381-1386 (September 1982).

[6]D. Zheng and R. L. Byer, "Proposed waveguide structure for laser driven electron accelerator," *Proc. Advanced Accelerator Concepts* (1994).

[7]C. M. Haaland, "Laser electron acceleration in vacuum," Opt. Commun. **114**, pp. 280-284 (1995).

[8]P. Sprangle, E. Esarey, J. Krall, and A. Ting, "Vacuum laser acceleration," submitted to Opt. Commun.

[9]A. M. Sessler, in *Laser Acceleration of Particles, AIP Conference Proceedings '91*.

[10]CLIC Study Group, in *Proceedings of the 1993 IEEE Particle Accelerator Conference* (IEEE, Piscataway, NJ, 1993), p. 540.

[11]C. E. Clayton, K. A. Marsh, A. Dyson, M. Everett, A. Lal, W. P. Leemans, R. Williams, and C. Joshi, Phys. Rev. Lett. **70**, p. 37 (1993).

[12]A. Piestrup, G. B. Rothbart, R. N. Fleming, and R. H. Pantell, J. Appl. Phys. **46**, p. 132 (1975).

[13]J. Bae, K. Furuya, H. Shirai, T. Nozokido, and K. Mizuno, "The inverse Smith-Purcell effect in the submillimeter wave region," Jpn. J. Appl. Phys. Vol. **27**, No. 3, pp. 408-412 (March 1988).

[14]J. D. Lawson, "Lasers and accelerators," *IEEE Trans. Nucl. Sci.* Vol. **NS-26**, No. 3 (June 1979).

[15]P. M. Woodward, *IEEE J.* **93**, p. 1554 (1947).

[16]J. A. Edighoffer and R. H. Pantell, "Energy exchange between free electrons and light in vacuum," J. Appl. Phys. **50**, p. 10 (October 1979).

[17]T. Hauser, W. Scheid, and H. Hora, "Acceleration of electrons by intensive laser pulses in vacuum," Phys. Lett. A **186**, pp. 189-192 (1994).

[18]H. Kogelnik and T. Li, "Laser beams and resonators," Applied Optics, Vol. **5**, No. 10, Oct. 1966.

[19]M. O. Scully, "A simple laser linac," Appl. Phys. B **51**, pp. 238-241 (1990).

[20]R. H. Pantell and M. A. Piestrup, "Free-electron momentum modulation by means of limited interaction length with light," Appl. Phys. Lett. **32**, p. 11 (June 1978).

[21]L. C. Steinhauer and W. D. Kimura, "A new approach for laser particle acceleration in vacuum," J. Appl. Phys. **72** , p. 8 (October 1992).

[22]E. Tanabe, M. Borland, M. C. Green, R. H. Miller, L. V. Nelson, J. N. Weaver, and H. Wiedemann, "A 2-MeV microwave thermionic gun," *SLAC-PUB-5054*, August 1989.

[23]L. W. Davis, "Theory of electromagnetic beams," Physical Rev. A, Vol. **19**, No. 3, (March 1979).

[24]A. E. Siegman, *Lasers* (University Science Books, 1986).

[25]A. Abramovici *et al.,* "LIGO: The Laser Interferometer Gravitational-wave Observatory," Science, Vol. **256**, pp. 325-333 (April 1992).

[26]P. R. Saulson, "Vibration isolation for broadband gravitational wave antennas," Rev. Sci. Instrum. **55** (8), pp. 1315-1320 (August 1984).

[27]D. F. Cioffi, "New Stanford facility squeezes high-energy electron beams," Physics Today (July 1994).

[28]U. Keller, "Ultrafast all-solid-state laser technology," Appl. Phys. B **58**, pp. 347-363 (1994).

[29]T. Day, E. K. Gustafson, and R. L. Byer, "Sub-hertz relative frequency stabilization of two-diode laser-pumped Nd:YAG lasers locked to a Fabry-Perot interferometer." *IEEE J. Quan. Elec.* Vol. **QE-18**, no. 4, pp. 1106-17 (1992).

[30]U. Amaldi, "Energy and luminosity requirements for the next generation of linear colliders," *AIP Conference Proceedings No. 156, Advanced Accelerator Concepts*, Madison, Wisconsin (1986).

[31]J. D. Jackson, *Classical Electrodynamics* (John Wiley & Sons, New York, 1975).

[32]A. E. Vlieks *et al.*, "Accelerator and RF system development for NLC," *Proceedings of the IEEE Particle Accelerator Conference*, Vol. **1**, Washington DC, pp. 620-622 (1993).

[33]H. J. Yeh and J. S. Smith, "Fluidic self-assembly of microstructures and its application to the integration of GaAs on Si," *Proceedings of the IEEE Micro Electro Mechanical Systems*, p. 279-284 (1994).

[34]M. H. Kiang, O. Solgaard, R. S. Muller, and K. Y. Lau, "Silicon-micromachined micromirrors with integrated high-precision actuators for external-cavity semiconductor lasers," to be published in *IEEE Phot. Tech. Lett.* (January 1996).